Spectrochimica Acta Part A: Molecular and Biomolecular Spectroscopy 139 (2015) 262–270

Contents lists available at ScienceDirect

Spectrochimica Acta Part A: Molecular and Biomolecular Spectroscopy

journal homepage: www.elsevier.com/locate/saa

# Synthesis, luminescence properties and EPR investigation of hydrothermally derived uniform ZnO hexagonal rods

A. Jagannatha Reddy [a,*], R. Hari Krishna [b,*], B.M. Nagabhushana [b], M.K. Kokila [c], H. Nagabhushana [d], C. Shivakumara [e], R.P.S. Chakradhar [f]

[a] Department of Physics, M.S. Ramaiah Institute of Technology, Bangalore 560 054, India
[b] Department of Chemistry, M.S. Ramaiah Institute of Technology, Bangalore 560 054, India
[c] Department of Physics, Bangalore University, Bangalore 560 056, India
[d] Centre for Advanced Materials Research, Tumkur University, Tumkur 572 103, India
[e] Solid State and Structural Chemistry Unit, Indian Institute of Science, Bangalore 560 012, India
[f] National Aerospace Laboratories (CSIR), Bangalore 560017, India

## HIGHLIGHTS

- Synthesized 1D hexagonal ZnO rods without the aid of any organic capping agents.
- Reaction temperature plays a crucial role in the formation of 1D hexagonal ZnO.
- Possible reasons for the observed morphological characteristics are discussed.
- Influence of reaction temperature on ZnO luminescence properties are explored.

## GRAPHICAL ABSTRACT

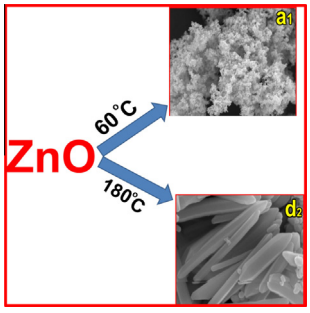


## ARTICLE INFO

*Article history:*
Received 7 May 2014
Received in revised form 19 October 2014
Accepted 20 November 2014
Available online 12 December 2014

*Keywords:*
Hydrothermal
Hexagonal rods
Photoluminescence
Thermoluminescence
Electron paramagnetic resonance

## ABSTRACT

One-dimensional (1D) zinc oxide (ZnO) hexagonal rods have been successfully synthesized by surfactant free hydrothermal process at different temperatures. It can be found that the reaction temperature play a crucial role in the formation of ZnO uniform hexagonal rods. The possible formation processes of 1-D ZnO hexagonal rods were investigated. The zinc hydroxide acts as the morphology-formative intermediate for the formation of ZnO nanorods. Upon excitation at 325 nm, the sample prepared at 180 °C show several emission bands at 400 nm (~3.10 eV), 420 nm (~2.95 eV), 482 nm (~2.57 eV) and 524 nm (~2.36 eV) corresponding to different kind of defects. TL studies were carried out by pre-irradiating samples with γ-rays ranging from 1 to 7 kGy at room temperature. A well resolved glow peak at ~354 °C was recorded which can be ascribed to deep traps. Furthermore, the defects associated with surface states in ZnO nanostructures are characterized by electron paramagnetic resonance.



## Introduction

In the recent past, developments in nanotechnology have led to the synthesis of semi conducting oxide nanostructures with unique optical and electrical properties, with great prospect of applying them as building blocks in electronic and photonic devices [1–5]. Fabrication of nanomaterials with controllable size and shape has

* Corresponding authors. Tel.: +91 9886537250, +91 9886434109.
*E-mail addresses:* ajreddy09@gmail.com (A.J. Reddy), rhk.chem@gmail.com (R.H. Krishna).

http://dx.doi.org/10.1016/j.saa.2014.11.088
1386-1425/

been of great scientific and technological interest due to their potential applications in nano-devices. ZnO is one of the most important II–VI semiconductors with unique properties and versatile applications. ZnO has a stable wurtzite structure with lattice spacing $a = 0.325$ nm and $c = 0.521$ nm consisting a number of planes composed of tetrahedrally coordinated $O^{2-}$ and $Zn^{2+}$ ions, which are stacked alternately along the $c$-axis. Because of its non-central symmetry, ZnO is piezoelectric, which is a key property in building electromechanical coupled sensors and transducers. ZnO is an environment friendly material and biocompatible which is desirable especially for biomedical applications. The excellent optical properties of ZnO such as a wide direct band gap (3.37 eV) and large exciton binding energy (60 meV) at room temperature endow ZnO as a promising material for short wavelength optoelectronic devices, self-powered nanosystems, sensors, ultraviolet lasers and field-emission devices [6–10].

The physical and chemical properties of nanomaterials vary as a function of size, shape and surface chemistry. Generally, the synthesis methods for ZnO nanostructures can be divided into two groups: wet-chemical/solution based and physical techniques based. Physical techniques typically require high temperatures and pressures. These methods result in low product yield and also energy and cost intensive. Wet-chemical/solution based methods are based on the hydrolysis of zinc complexes at elevated or room temperatures. These methods provide convenient, facile manipulation, potential for scale-up and a lower temperature pathway for the fabrication of the desired ZnO nanostructures. The growth direction can be controlled with various additives in these methods.

A large number of techniques like thermal decomposition, chemical vapor deposition, laser ablation, hydrothermal synthesis, sputtering, combustion, sol–gel process etc., [11–16] have been used for synthesis of many interesting morphological nanostructures of ZnO including nanoflowers, nanobelts, nanobridges, nanonails, nanoribbons, nanowires and nanorods. Compared with other preparation methods, hydrothermal synthesis is often used because it is carried out in a mild way at low temperature and allows control of size, morphology and crystallinity by tuning the experimental variables such as temperature, pressure, duration of process, concentration of chemical species and pH of solution. Hydrothermal synthesis is an environment friendly, low-temperature, low-cost method and is thus of interest for practical applications. Herein, we have synthesized rods, wires and flakes-like ZnO nanostructures by organic-free hydrothermal process at different temperatures and report TL and EPR study of the defects associated with surface states in ZnO nano-structures.

## Experimental

### *Hydrothermal synthesis*

Hydrothermal synthesis was carried out using general purpose autoclaves made of stainless-steel provided with Teflon liners of a capacity of 30 ml. The experimental duration was maintained at 16 h with an autogenous pressure in all experiments. The molarity and PH of the raw material was kept constant in order to study the effect of experimental temperature in the hydrothermal reaction on the resultant product and in turn the morphology and luminescence properties.

The procedure employed for preparing ZnO nanostructures is as follows: in a typical synthesis, 2.97 g of zinc nitrate [$Zn(NO_3)_2$: $6H_2O$], 20 ml of double distilled water and 20 ml of ethanol (absolute) are taken in Teflon liner. 4.48 g of solid NaOH was slowly added into the mixture and stirred vigorously for a few minutes until it becomes highly viscous and colorless transparent solution. Later, the liner was kept inside the autoclave and sealed firmly. The autoclave assembly was then placed inside a furnace provided with a temperature programmer. The temperature of the autoclave was slowly raised to 60 °C and held for 16 h. After the experimental run, the autoclave was cooled to room temperature and the liner assembly was taken out. The contents were first washed with doubled-distilled water and then with ethanol and centrifuged repeatedly to remove all the excess acid in the resultant products. The products were then dried at 60 °C for 3 h in a dust-proof hot-air oven. The hydrothermal synthesis was repeated by setting the furnace temperature at different values (100, 140, 180, 220 and 260 °C). The flow chart of hydrothermal synthesis is shown in the Fig. 1. The resultant products were then subjected to a systematic characterization using different analytical techniques and their photoluminescence (PL) and thermoluminescence (TL) properties were studied.

### *Instruments used*

The powder X-ray diffraction studies were carried out using PANalytical X'pert Pro, Almelo, (The Netherland) with Cu Kα radiation ($\lambda = 1.541$ Å). The surface morphology of the samples was examined using Scanning electron microscopy (JEOL JSM 840A) by sputtering technique with gold as covering contrast material. Fourier transform infrared spectroscopy (FTIR) spectrum was taken using a Perkin–Elmer Rx1 instrument. The UV–Vis spectrum was recorded on a UV-3101 Shimadzu Visible spectrometer. The photoluminescence studies were carried out using a Perkin–Elmer LS-55 luminescence spectrophotometer equipped with Xe lamp. The synthesized samples were irradiated with different doses of γ-rays in the range 1–7 kGy from Co-60 source at room temperature. After the desired exposure, TL glow curves were recorded on a Nucleonics TLD reader taking 5 mg of the sample each time at a heating

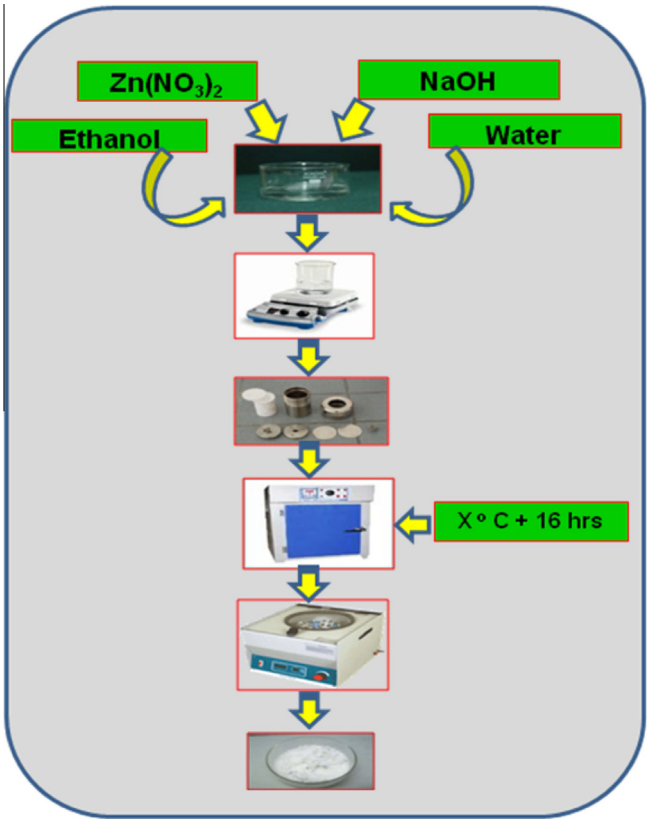


**Fig. 1.** Flow chart of hydrothermal synthesis.

rate of 6.7 °C $s^{-1}$. The EPR spectrum was recorded at room temperature using a JEOL-FE-1X EPR spectrometer operating in the X-band frequency (≈9.205 GHz) with a field modulation frequency of 100 kHz. A powdered specimen of 100 mg was taken in a quartz tube for EPR measurements. The magnetic field was scanned from 0 to 500 mT and the microwave power used was 10 mW.

## Results and discussion

### *Powder X-ray diffraction (PXRD) analysis*

PXRD pattern has been measured for assessing the overall structure and phase purity of the samples. Fig. 2 shows the PXRD patterns acquired from the samples prepared at 60–260 °C for 16 h. All the diffraction peaks in the pattern corresponding to (100), (002), (101), (102), (110), (103), (200), (112) and (201) directions were indexed as the pure hexagonal phase of ZnO with space group $P6_3mc$. It is found that there are weak diffraction peaks at 44° and 52°, these are attributed to the presence of trace amounts of $Zn_5(NO_3)_2(OH)_8{\cdot}2H_2O$ (JCPDS: 72-0627). The reasons why these peaks are in only some of the samples are hitherto unknown. The deviation from perfect crystallinity leads to broadening of the diffraction peaks. The broadening of the diffraction peaks is an indication that the synthesized materials are in nanometer regime, which is in accord with the high-magnification SEM observations. The crystallite size and lattice strain can be extracted from X-ray peak width analysis. Crystallite size is a measure of the size of coherently diffracting domains. Lattice strain is a measure of the distribution of lattice constants arising from crystal imperfections such as lattice dislocations, contact or sinter stresses, stacking faults and coherency stresses. Crystallite size and lattice strain affect the X-ray diffraction peak in different ways. Both these effects increase the peak width and intensity accordingly.

On the full width at half-maximum (FWHM) of (100), (002) and (101) diffraction peaks, the crystallite sizes of ZnO nanostructures are estimated from the Debye–Scherrer's equation. The average crystallite size is found to be in the range of ~26–45 nm depending on the growth condition.

The lattice parameters and unit cell volumes for hexagonal ZnO nanoparticles are calculated from the lattice geometry equations,

$$\frac{1}{d^2} = \frac{4}{3} \times \frac{h^2 + hk + k^2}{a^2} + \frac{l^2}{c^2} \quad (1)$$

$$V = \frac{\sqrt{3}a^2c}{2} = 0.866a^2c \quad (2)$$

where $a$ and $c$ are the lattice parameters and $h$, $k$, and $l$ are the Miller indices and $d_{hkl}$ is the interplanar spacing, which can be calculated from Bragg's law:

$$2d \sin\theta = n\lambda \quad (3)$$

The lattice parameters calculated ($a$ = 3.249 and $c$ = 5.206 Å) and unit cell volume ($V \approx 47.5$ (Å)$^3$) are consistent with the standard data base of wurtzite structural ZnO (JCPDS card No. 36-1451).

### *Fourier transform infrared spectroscopy (FTIR)*

To investigate the surface adsorption and functional groups present in hexagonal shaped nanostructures synthesized at 180 °C, its FTIR spectrum was recorded in the range of 400–4000 $cm^{-1}$ (Fig. 3). It has been reported that two surfaces, i.e., polar and non-polar, behave differently in ZnO system. Assignment of hydroxyl and metal–oxygen bands in ZnO has been made by several workers [17–19]. The broad band at 3420 and 2360 $cm^{-1}$ indicates O–H stretching of $H_2O$ and the bands at 1380 and 842 $cm^{-1}$ are ascribed to O–H bending. The transmittance peak at 1455 $cm^{-1}$ is ascribed to $NO_3^-$ which originates from the unreacted metal nitrates used for synthesis. The sharp intense transmittance peak at 415 $cm^{-1}$ is ascribed to Zn–O stretching vibration that confirms the formation of ZnO. This result also confirms the formation of ZnO phase with trace amounts of precursor impurities or intermediate compound $Zn_5(NO_3)_2(OH)_8{\cdot}2H_2O$. This

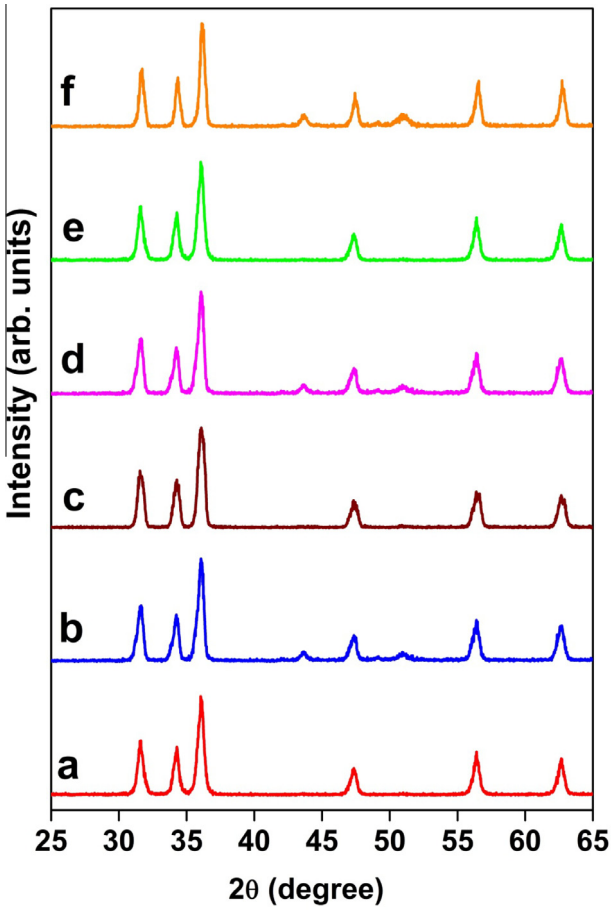


**Fig. 2.** PXRD patterns of ZnO nanostructures synthesized hydrothermally at different temperatures (a) 60 °C (b) 100 °C (c) 140 °C (d) 180 °C (e) 220 °C (f) 260 °C.

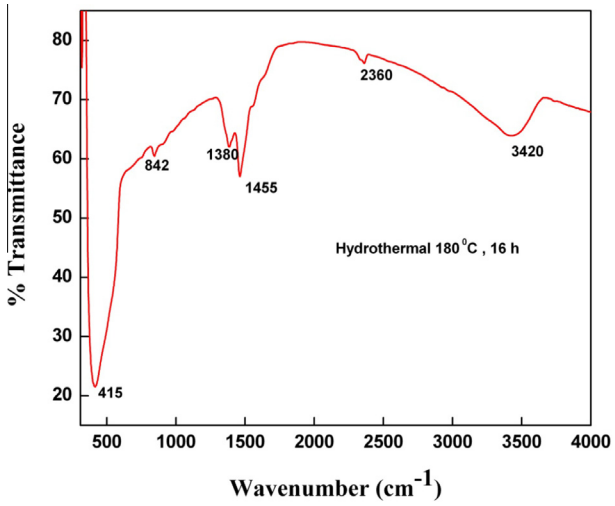


**Fig. 3.** FTIR spectrum of ZnO nanostructures synthesized hydrothermally at 180 °C.

is consistent with XRD studies, which reveal the formation of wurtzite phase and presence of $Zn_5(NO_3)_2(OH)_8{\cdot}2H_2O$.

*Scanning electron microscopy (SEM)*

It is reported that there are different parameters namely, hydrothermal temperature, duration, pH value and capping agent; that can influence the growth pattern and characteristics of the resulting ZnO products under non-equilibrium kinetic growth conditions in the solution-based approach [7]. In our experiment, the effects of hydrothermal temperature on the morphology and size distribution of the samples were investigated using the SEM technique. Fig. 4 shows the SEM images of the ZnO samples prepared at different hydrothermal temperatures. Fig. 4($a_1$, $a_2$) display SEM images of the sample prepared at 60 °C and it consist of a large quantity of quasi-hexagonal shaped structures with varying sizes in the 50–100 nm range. Fig. 4($b_1$, $b_2$) and ($c_1$, $c_2$) show the SEM images of ZnO prepared at 100 and 140 °C respectively. Careful examination of SEM images reveal that the sample is composed of hexagonal shaped nanoparticles and some nanobelts or nanorods with the width of about 250 nm and numerous wire structures with the diameter of about 10 nm. All of them have the length of few micrometers. Fig. 5($d_1$) and ($d_2$) shows the SEM images of ZnO at 180 °C revealing the presence of hexagonal shaped nanorods and nanoparticles dual structure. The hexagonal shaped rods were found to have smooth, uniform surfaces with an acute tip and varying diameters in the 100–200 nm range and few micrometers in length. The sample at 220 °C (Fig. 5($e_1$, $e_2$)) also exhibit the similar morphology with large quantity of particles sticking to the nanorods. With the further increase in hydrothermal temperature to 260 °C, the sample exhibits flake-like morphology with interconnected discrete nanocrystallites forming a loose porous structure (Fig. 5($f_1$, $f_2$)). The nanopores among the aggregated ZnO nanocrystallites may result from the evolution of $CO_2$ and $H_2O$ gases due to thermal decomposition of the precursor during heat treatment.

The formation of hexagonal shaped nanorods with an acute tip can be explained as shown in the Fig. 6. Growth mechanism of formation of hexagonal shaped nanorods with an acute tip at 180 °C is explained below. ZnO is a polar crystal whose positive polar plane is rich in Zn and the negative polar plane is rich in O. Several growth mechanisms [20,21] have been proposed for aqueous chemical solution deposition. Among many growth mechanisms

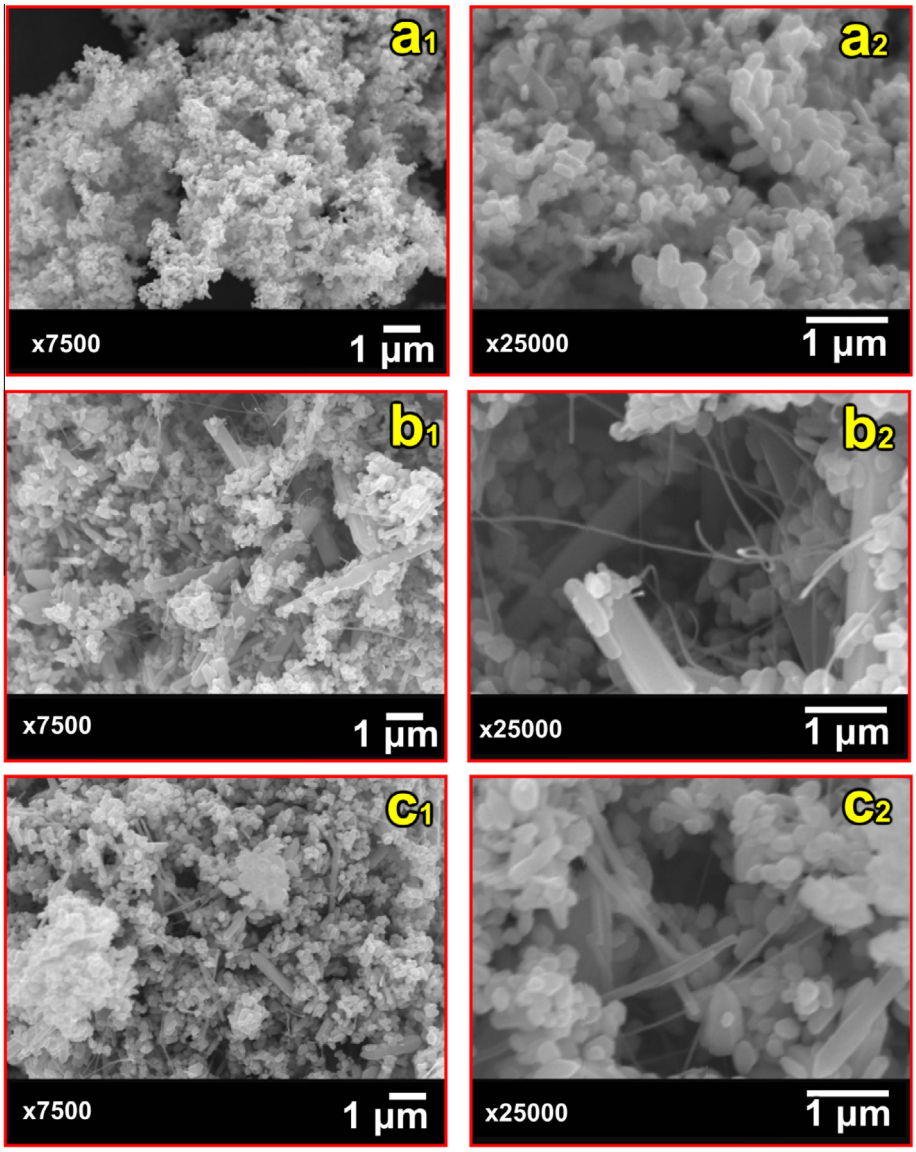


**Fig. 4.** SEM micrographs with two different magnifications of ZnO powders prepared at different hydrothermal temperatures ($a_1$, $a_2$) – 60 °C, ($b_1$, $b_2$) – 100 °C, ($c_1$, $c_2$) – 140 °C.

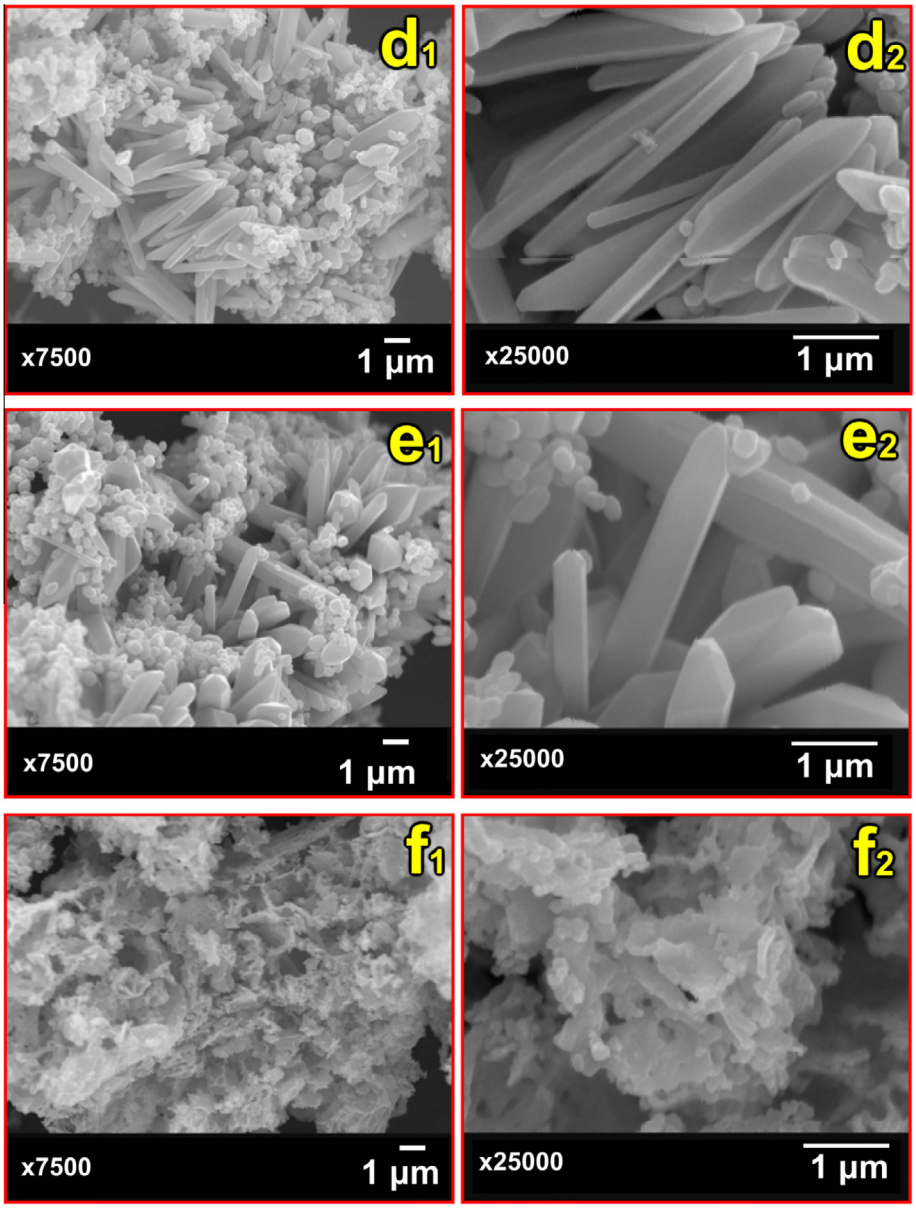


**Fig. 5.** SEM micrographs with two different magnifications of ZnO powders prepared at different hydrothermal temperatures, ($d_1$, $d_2$) – 180 °C, ($e_1$, $e_2$) – 220 °C, ($f_1$, $f_2$) – 60 °C.

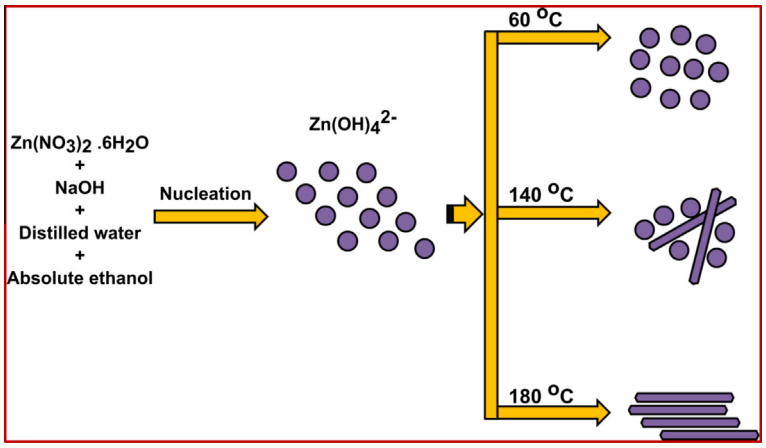


**Fig. 6.** Mechanism/formation of nanorods.

proposed the most familiar and important growth path for a single crystal is the Ostwald ripening process [21]. This is a spontaneous process that occurs because larger crystals are more energetically favored than smaller crystals. According to this process, kinetically favored tiny crystallites nucleate first in supersaturated medium and are followed by the growth of thermodynamically favored larger particles [22]. The aqueous solutions of zinc nitrate and ethanol in presence of NaOH can produce the following chemical reactions. The concentration of reactants and reaction time plays a vital role for the formation of ZnO nanostructure since $OH^-$ is strongly related to the reaction that produces nanostructures. In present work since concentration of reactants were kept constant, growth path can be explained by the variable, reaction temperature.

$$Zn(NO_3)_2 \rightarrow Zn^{2+} + 2NO^{3-} \quad (4)$$

$$2C_2H_5OH + 2NaOH \rightarrow 2C_2H_5ONa + 2H_2O \quad (5)$$

$$2H_2O \leftrightarrow H_3O^+ + OH^- \quad (6)$$

$$Zn^{2+} + 2OH^- \leftrightarrow Zn(OH)_2 \quad (7)$$

$$Zn(OH)_2 \rightarrow ZnO + H_2O \quad (8)$$

The colloidal $Zn(OH)_2$ clusters so formed in solution will act as nuclei for the growth of ZnO nanorods. During the hydrothermal growth process, the $Zn(OH)_2$ dissolves with increasing temperature. When the concentrations of $Zn^{2+}$ and $OH^-$ reach the critical value of the supersaturation of ZnO, fine ZnO nuclei form spontaneously in the aqueous complex solution. When the solution is supersaturated, nucleation begins. Further, ZnO nanoparticles combines together to reduce the interfacial free energy. This is because the molecules at the surface are energetically less stable than the ones already well orderly formed and packed in the interior. In our experiments we found that the concentration of $Zn^{2+}$ and $OH^-$ has attained critical value and incorporation of growth units into crystal lattice of the hexagonal nanorods by dehydration took place when deposition temperature was 180 °C. When the temperature was maintained at less than 180 °C the $OH^-$ concentration could not attain the critical value to form the enough $Zn(OH)_2$ growth units to form ZnO nanorods that resulted in the tiny hexagonal particles.

*Photoluminescence (PL) spectrum*

Fig. 7 illustrates the room temperature photoluminescence spectrum of hydrothermally synthesized ZnO nanostructures with experimental temperature of 180 °C at excitation wavelength of 325 nm. Several emission bands, including band edge UV emission at 400 nm (~3.10 eV) and defect related violet emission at 420 nm (~2.95 eV), blue–green emission at 482 nm (~2.57 eV) and green emission at 524 nm (~2.36 eV) were observed. In PL spectrum of ZnO band at 400 nm, could be attributed to free exciton recombination through exciton–exciton collisions, [23] corresponding to the near-band-gap emission (NBE), which corresponds to an energy gap of 3.10 eV.

The broad emission peak is associated with the various deep-level defects, such as zinc vacancy ($V_{Zn}$), zinc interstitial ($Zn_i$), oxygen interstitial ($O_i$), oxygen vacancy ($V_o$), and single ionized oxygen vacancies in ZnO lattice [24,25]. To explain these emissions, different hypotheses have been reported in the literature; nevertheless, the origin of these emissions remains still unclear and debatable. The visible emission which is referred to as deep-level emission and attributed to recombination of electrons deeply trapped in oxygen vacancies and zinc interstitials, with photo generated holes [26–28]. The origin of defect related violet emission centered at 2.95 eV (~420 nm) is ascribed to an electron transition from a shallow donor level of neutral zinc interstitial ($Zn_i$) to the top level of the valence band [29]. The blue emission bands appearing at around at 470 nm have rarely been observed. Zeng et al. [30] and Shi et al. [31] reported that the green or blue emission bands can be excited only by energies lower than the band-gap for as-grown and annealed ZNAs. Zeng et al. attributed this kind of emission to Zn interstitials, while Shi et al. proposed that this type of emission is due to oxygen vacancies. These two kinds of defects are easily formed during hydrothermal treatment after oxygen-poor thermal treatment. Therefore, we can attribute the 495 nm emission peak excited by 325 nm light to either Zn interstitials or oxygen vacancies, or a combination of both, which is in agreement with the previous results. The green emission is attributed to the recombination of electrons trapped in singly ionized oxygen vacancies ($V_o$) with photogenerated holes [32]. Heo et al. [33] have reported that green emission is commonly observed in ZnO samples prepared in oxygen deficient environments resulting in vacancy of oxygen and they have attributed it to donor $V_o$ –acceptor $V_{Zn}$ recombination. Wen et al. [34] reported green emission in ZnO crystal synthesized by a hydrothermal method with hydrazine. They explained that the green emission is due to excess Zn which comes from the reduction of $Zn^{2+}$ ions in the reaction process. In the present study, EPR results for the ZnO nanostructures have also manifested that the $V_o$ centers are the predominant defects in the sample.

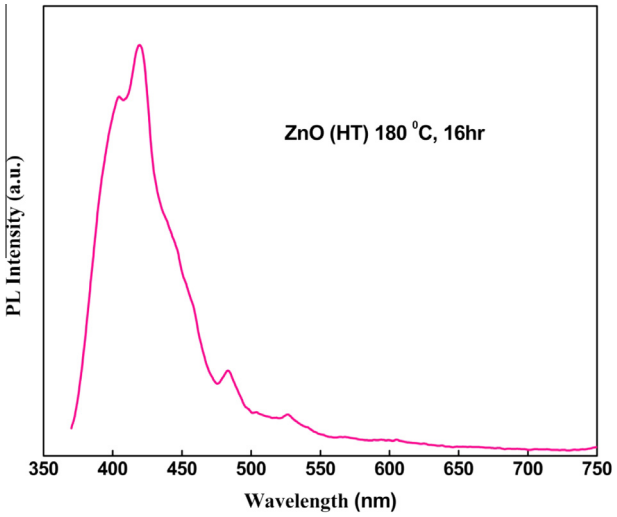


**Fig. 7.** PL spectrum of ZnO nanostructures synthesized hydrothermally at 180 °C with excitation wavelength of 325 nm.

*Thermoluminescence (TL) study*

Significant advancements have been made in thermo luminescence (TL) experiments during last couple of decades. However, the most important application of TL lies in radiation dosimetry, which spans areas of health physics and other biological sciences, radiation protection and personnel monitoring. TL experiments are equally helpful in defects and impurities related studies in solids. With the advent of nanotechnology, there is still a considerable amount of research for new nanocrystalline phosphor materials with better TL and dosimetric properties. The importance of nanocrystalline materials has increased tremendously because of the enhanced optical, electronic and structural properties than their bulk counterparts due to quantum size effect and an increased surface to volume ratio. TL glow curves of hydrothermally prepared ZnO nanostructures with experimental temperature of 180 °C and gamma ($\gamma$) irradiated for a dose range of 1–7 kGy at a heating rate of 6.7 °C $s^{-1}$ are shown in the Fig. 8.

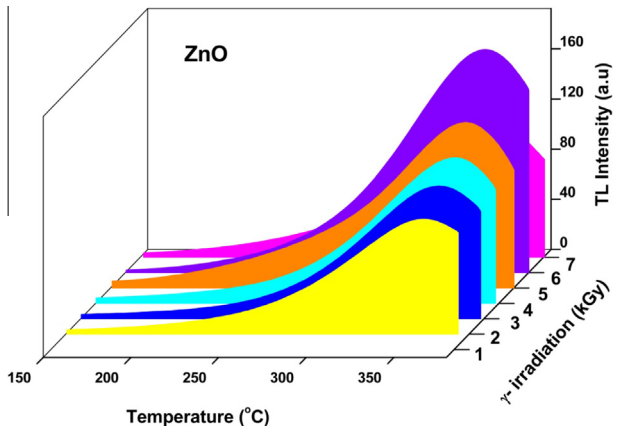


**Fig. 8.** TL glow curves of ZnO nanostructures synthesized hydrothermally at 180 °C.

γ-Irradiation creates F and $F^+$ type centers and $F^+$ type centers are formed when an electron is trapped at vacant oxygen interstitial surface sites. Further vacant interstitial surface sites can also trap holes during irradiation. Since the mobility of holes at RT is quite high, these centers will decay very fast. In combustion derived ZnO nano structures studied by the same authors [35], a well resolved broad single glow peak at ~343 °C was observed, which is attributed to the recombination of charge carriers released form the surface states associated with oxygen defects, mainly interstitial oxygen ion centers. In the present study, a broad single glow peak at ~354 °C was observed for all the dosages. It can be seen that the shapes of the TL curves recorded for different dosages are very similar, indicating that the physical properties of the traps are about the same. The broad shape of the TL peak suggests the distribution of traps in the band gap of nanostructures. Fig. 9 shows the variation of glow peak intensity with γ-irradiation dose. The glow peak intensity increased with increase of gamma dose from 1 to 6 kGy and then decreased for 7 kGy without change in glow curve shape. The increase in intensity of TL glow peak with irradiation dose can be understood by the fact that more and more traps responsible for the glow peak are getting filled with the increase of irradiation dose and subsequently these traps release the charge carriers on thermal stimulation to finally recombine with their counterparts.

The heating rate is a dynamic parameter which influences the characteristics of the TL glow-peaks. The influence of different heating rates on ZnO exposed to 5 kGy γ-radiation has been investigated. The TL glow curves at heating rates of 5, 7.5, 10 and 12.5 °C/s are shown in Fig. 10. It is worth noticing that with increasing in heating rate the area under the glow curve decreases although not significant and also the glow curve shifts to higher temperature side. This may be attributed to the difference in thermal release of electrons that depends on half-life at different temperatures. When the heating rate is low $\beta 1$ the sample under test spends enough time at temperature $T_1$ so that an amount of thermal release of electrons depends on the half life time at this temperature. As the heating rate increases to $\beta 2$ from $\beta 1$, the time spent by the phosphor at the same temperature $T_1$ decreases and therefore the thermal release of electrons also decreases. So the higher temperature $T_2$ is required for the same amount of thermal release to take place at $\beta 2$. In this way the whole glow curve and hence the glow peak temperature shifts to right side as the heating rate increases in a manner depending on the half-life and the time spent at each temperature [36].

The trapping parameters of ZnO irradiated with various γ-doses obtained using peak shape method is given in Table 1. The following empirical formulae are used to estimate trapping parameters using the Chen's peak shape method [37]:

*The activation energy (E)*

$$E_\alpha = c_\alpha\left(\frac{KT_m^2}{\alpha}\right) - b_\alpha(2KT_m) \tag{9}$$

where $\alpha = \tau$, $\delta$, and $\omega$ $\tau = T_m - T_1$, $\delta = T_2 - T_m$ and $\omega = T_2 - T_1$

$$C_\tau = 1.51 + 3.0(\mu_g - 0.42), \quad b_\tau = 1.58 + 4.2(\mu_g - 0.42) \tag{10}$$

$$C_\delta = 0.976 + 7.3(\mu_g - 0.42), \quad b_\delta = 0 \tag{11}$$

$$C_\omega = 2.52 + 10.2(\mu_g - 0.42), \quad b_\omega = 1 \tag{12}$$

*Frequency factor (s)*

Once $E$ and $b$ are known, frequency factor ($s$) can be evaluated

$$s = \frac{\beta E}{kT_m^2}\exp\left\{\frac{E}{kT_m^2}\right\}[1 + (b-1)\Delta_m]^{-1} \tag{13}$$

where $\beta$ is the linear heating rate, $b$ is the order of kinetics and $\Delta = \frac{2kT}{E}; \Delta_m = \frac{2kT_m}{E}$.

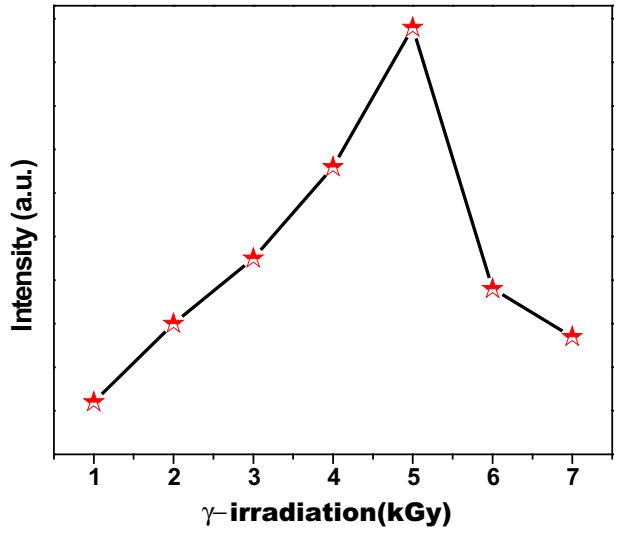


**Fig. 9.** Variation of TL intensity with γ-irradiation dose.

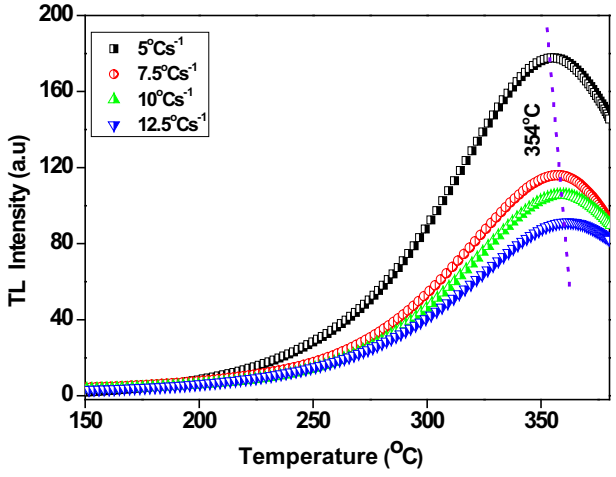


**Fig. 10.** TL glow curves of ZnO nanostructures synthesized hydrothermally at 180 °C at different heating rates.

**Table 1**
Estimated trap parameters of ZnO prepared at 180 °C for different heating rates.

| Heating rate (°C $s^{-1}$) | Peak | $T_m$ (°C) | Order of kinetics ($b$) | Balarin parameter | Activation energy (eV) | | | | Frequency factor ($s^{-1}$) |
|---|---|---|---|---|---|---|---|---|---|
| | | | | | $E_\tau$ | $E_\delta$ | $E_\omega$ | $E_{ave}$ | |
| 5 | 1 | 289 | 2 | 0.98 | 1.15 | 1.21 | 1.18 | 1.18 | 4.8E+11 |
| | 2 | 327 | 2 | 1.03 | 1.63 | 1.62 | 1.63 | 1.63 | 6.7E+14 |
| | 3 | 354 | 2 | 1.00 | 2.16 | 2.11 | 2.15 | 2.14 | 2.8E+18 |
| 7.5 | 1 | 265 | 2 | 0.96 | 0.34 | 0.46 | 0.40 | 0.40 | 2.2E+05 |
| | 2 | 342 | 2 | 0.94 | 1.43 | 1.47 | 1.46 | 1.46 | 1.1E+13 |
| | 3 | 370 | 2 | 0.93 | 1.95 | 1.95 | 1.96 | 1.95 | 3.2E+16 |
| 10 | 1 | 268 | 2 | 1.01 | 0.41 | 0.52 | 0.47 | 0.47 | 1.1E+05 |
| | 2 | 335 | 2 | 1.04 | 0.97 | 1.04 | 1.01 | 1.01 | 1.9E+09 |
| | 3 | 370 | 2 | 0.81 | 1.34 | 1.39 | 1.38 | 1.37 | 6.1E+11 |
| 12.5 | 1 | 281 | 2 | 1.17 | 0.51 | 0.59 | 0.55 | 0.55 | 5.4E+05 |
| | 2 | 309 | 2 | 1.00 | 0.99 | 1.05 | 1.03 | 1.03 | 7.4E+09 |
| | 3 | 367 | 2 | 0.76 | 1.17 | 1.17 | 1.15 | 1.15 | 9.6E+09 |

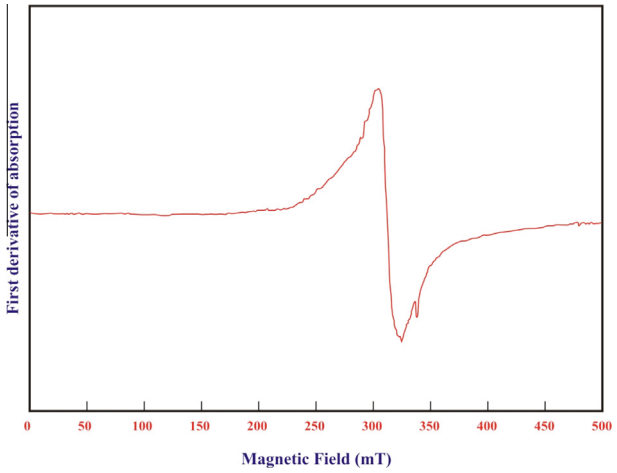


**Fig. 11.** EPR spectrum of ZnO nanostructures synthesized hydrothermally at 180 °C.

*Order of kinetics*

To determine the order of kinetics ($b$), the form factor or symmetry factor

$$\mu_g = \frac{T_{2-T_m}}{T_{2-T_1}} \tag{14}$$

which involves calculation of $T_1$ and $T_2$ ($T_1$ and $T_2$ are the temperatures corresponding to the half of the maximum intensities on either side of the glow peak maximum temperature ($T_m$)). The nature of the kinetics can be found by the form factor. Theoretically the value of geometrical form factor ($\mu_g$), close to 0.42, for first order kinetics and value can be 0.52 for second order.

The estimated kinetic parameters for ZnO irradiated with various γ-doses obtained using peak shape method is given in Table 1.

*Electron paramagnetic resonance (EPR) study*

Electron paramagnetic resonance (EPR) is a powerful tool to monitor the paramagnetic charge states of vacancies/defects in ZnO. Fig. 11 shows the X-band EPR spectrum of ZnO nanostructures synthesized hydrothermally at 180 °C. The EPR spectrum shows a broad resonance signal with effective g value of 2.107 along with a sharp signal at $g = 1.941$. This indicates that several kinds of defects are present in the sample. In the EPR spectrum of ZnO nanocrystalline powder prepared by combustion method [38–40], sharp resonance signals at $g = 1.994$ and $g = 2.007$ and broad resonance signals at $g = 2.540$, $g = 2.145$ and $g = 1.775$ are observed. In the present study, the resonance signals at $g = 1.941$ is sharp and can be assigned to $V_0^+$ singly ionized oxygen vacancy. The other resonance signal at $g = 2.107$ is broad and can be attributed to Zn vacancy.

*Conclusions*

Zinc oxide (ZnO) hexagonal rods have been successfully synthesized by surfactant free hydrothermal process at different temperatures. The zinc hydroxide acts as the morphology-formative intermediate for the formation of ZnO. We found that the concentration of $Zn^{2+}$ and $OH^-$ has attained critical value and incorporation of growth units into crystal lattice of the hexagonal nanorods by dehydration took place when deposition temperature was 180 °C. Upon excitation at 325 nm, the sample prepared at 180 °C show several emission bands corresponding to different kind of defects. A well resolved TL glow peak at ~354 °C was recorded which can be ascribed to deep traps. In the EPR study, the resonance signals at $g = 1.941$ is sharp and can be assigned to $V_0^+$ singly ionized oxygen vacancy. The other resonance signal at $g = 2.107$ is broad and can be attributed to Zn vacancy.

## Acknowledgements

AJR and RHK are grateful to the Management and Principal of M. S. Ramaiah Institute of Technology, Bangalore, for their constant support and encouragement. Authors are also thankful to Dr. J. L. Rao, Retd. Professor, Department of Physics, S.V. University, Tirupathi, for his valuable suggestions and help in EPR measurements.

## References

[1] C.N.R. Rao, F. L Deepak, G. Gundiah, A. Govindaraj, Prog. Solid State Chem. 31 (2003) 5–147.
[2] W. Guo, T. Liu, H. Zhang, R. Sun, Y. Chen, W. Zeng, Z. Wang, Sen. Actuators, B: Chem. 166 (2012) 492–499.
[3] W. Peng, S. Qu, G. Cong, Z. Wang, Cryst. Growth Des. 6 (2006) 1518–1522.
[4] P. Nguyen, H.T. Ng, T. Yamada, M.K. Smith, J. Li, J. Han, M. Meyyappan, Nano Lett. 4 (2004) 651–657.
[5] M. Law, J. Goldberger, P. Yang, Annu. Rev. Mater. Res. 34 (2004) 83–122.
[6] Z.L. Wang, Adv. Funct. Mater. 18 (2008) 1–7.
[7] M.H. Huang, Y. Wu, H. Feick, N. Tran, E. Weber, P. Yang, Adv. Mater. 13 (2001) 113–116.
[8] H. Cao, J.Y. Xu, D.Z. Zhang, S.H. Chang, S.T. Ho, E.W. Seelig, X. Liu, R.P.H. Chang, Phys. Rev. Lett. 84 (2000) 5584–5587.
[9] Y.W. Zhu, H.Z. Zhang, X.C. Sun, S.Q. Feng, J. Xu, Q. Zhao, B. Xiang, R.M. Wang, D.P. Yu, Appl. Phys. Lett. 83 (2003) 144–146.
[10] R. Zhang, S. Kumar, S. Zou, L.L. Kerr, Cryst. Growth Des. 8 (2008) 381–383.
[11] H. Qian, G. Lin, Y. Zhang, P. Gunawan, R. Xu, Nanotechnology 18 (2007) 1–9.
[12] Y.J. Lee, D.S. Ruby, D.W. Peters, B.B. McKenzie, J.W.P. Hsu, Nano Lett. 8 (2008) 1501–1505.

[13] M. Yang, G. Pang, L. Jiang, S. Feng, Nanotechnology 17 (2006) 206–212.
[14] M.N.R. Ashfold, R.P. Doherty, N.G. Ndifor-Angwafor, D.J. Riley, Y. Sun, Thin Solid Films 515 (2007) 8679–8683.
[15] R. Teki, T.C. Parker, H. Li, N. Koratkar, T.M. Lu, S. Lee, Thin Solid Films 516 (2008) 4993–4996.
[16] S.W. Kang, S.K. Mohanta, Y.Y. Kim, H.K. Cho, Cryst. Growth Des. 8 (2008) 1458–1460.
[17] J. Strunk, K. Kahler, X. Xia, Martin Muller, Surf. Sci. 603 (2009) 1776–1783.
[18] Y. Wang, C. Woll, Surf. Sci. 603 (2009) 1599–1602.
[19] G. Ghiotti, A. Chiorino, F. Boceuzi, Surf. Sci. 287 (1993) 228–234.
[20] H. Zhang, D. Yang, Y.J. Yi, X.Y. Ma, J. Xu, D.L. Que, J. Phys. Chem. B 108 (2004) 3955–3958.
[21] O. Krichershy, Stavan, J. Phys. Rev. Lett. 70 (1993) 1473–1475.
[22] D. Polsongkrama, P. Chamninok, S. Pukird, L. Chowb, O. Lupan, G. Chai, H. Khallaf, S. Park, A. Schulte, Physica B 403 (2008) 3713–3717.
[23] V.A. Fonoberov, K.A. Alim, A.A. Balandin, F. Xiu, J. Liu, Phys. Rev. B: Condens. Matter Mater. Phys. 73 (2006) 165317.
[24] K. Vanheusden, W.L. Warren, C.H. Seager, D.R. Tallant, J.A. Voigt, B.E. Gnade, J. Appl. Phys. 79 (1996) 7983–7990.
[25] Y.J. Lin, C.-L. Tsai, Y.-M. Lu, C.-J. Liu, J. Appl. Phys. 99 (2006) 093501.
[26] L.T. Tseng, J.B. Yi, X.Y. Zhang, G.Z. Xing, H.M. Fan, T.S. Herng, X. Luo, M. Ionescu, J. Ding, S. Li, AIP Adv. 4 (2014). 067117-7.
[27] Jeremy Smith, Arash Akbari-Sharbaf, Matthew J. Ward, Michael W. Murphy, Giovanni Fanchini, Tsun Kong Sham, J. Appl. Phys. 113 (2013) 093104–93106.
[28] Sayan Bayan, Purushottam Chakraborty, Appl. Surf. Sci. 303 (2014) 233–240.
[29] X.M. Fan, J.S. Lian, L. Zhao, Y. Liu, Appl. Surf. Sci. 252 (2005) 420–424.
[30] H. Zeng, G. Duan, Y. Li, S. Yang, X. Xu, W. Cai, Adv. Funct. Mater. 20 (2010) 561–572.
[31] Shi Shaobo, J. Xu, X. Zhang, J. Appl. Phys. 109 (2011) 103506.
[32] S. Baek, J. Song, S. Lim, Physica B 399 (2007) 101–104.
[33] Y.W. Heo, D.P. Norton, S.J. Pearton, J. Appl. Phys. 98 (2005) 1–6.
[34] F. Wen, W. Li, J. Moon, J. Kima, Solid State Commun. 135 (2005) 34–37.
[35] A.J. Reddy, M.K. Kokila, H. Nagabhushana, J.L. Rao, C. Shivakumara, B.M. Nagabhushana, R.P.S. Chakradhar, Spectrochim. Acta A 81 (2011) 59–63.
[36] M.T. Jose a, S.R. Anishia, O. Annalakshmi, V. Ramasamy, Radiat. Meas. 46 (2011) 1026–1032.
[37] R. Chen, Y. Kirsh, Analysis of Thermally Stimulated Process, Pregamon, Oxford, 1981.
[38] J.R. Smith, W.H. Vehse, Phys. Lett. A 31 (1970) 147–148.
[39] J.M. Meese, D. Galland, Solid State Commun. 11 (1972) 1547–1550.
[40] V. Soriano, D. Galland, Phys. Status Solidi B 77 (1976) 739–743.